

Fracture toughness evaluation of a nuclear graphite with non-linear elastic properties by 3D imaging and inverse finite element analysis

Hongniao Chen^{a,b,*}, Jie Shen^{a,c}, Daniel Scotson^{b,d}, Xiaochao Jin^{b,e}, Houzheng Wu^f, T. James Marrow^{b,*}

^a Research Center of Space Structures, Guizhou University, Guizhou, Guiyang 550025, China

^b Department of Materials, University of Oxford, Oxford OX1 3PH, United Kingdom

^c College of Civil Engineering, Guizhou University, Guizhou, Guiyang 550025, China

^d Henry Royce Institute, University of Manchester, Manchester M13 9PL, United Kingdom

^e State Key Laboratory for Strength and Vibration of Mechanical Structures, School of Aerospace Engineering, Xi'an Jiaotong University, Xi'an 710049, China

^f Department of Materials, Loughborough University, Epinal Way, Loughborough LE11 3TU, United Kingdom

ARTICLE INFO

Keywords:

Graphite
DVC
X-ray tomography
Fracture toughness
Small specimen testing
Non-linear elasticity

ABSTRACT

Effective small specimen tests are needed to obtain fracture toughness and elastic properties as the limited availability of irradiated graphite restricts the quantity and dimensions of test specimens. Both properties have been evaluated simultaneously in a crack propagation test with the double cleavage drilled compression (DCDC) specimen geometry of a fine-grained graphite (SNG742) that has non-linear elastic properties in the unirradiated condition. Three-dimensional displacement fields were obtained by digital volume correlation of in situ laboratory X-ray computed tomographs, and the 3D crack geometry (crack tip position, crack opening displacements and angle) was determined objectively by a wavelet variance method. The tensile softening of the Young modulus was determined by inverse analysis of the strain field using the finite element model updating (FEMU) method. The strain energy release rate of the quasi-static propagating crack was calculated using the contour integral method in a finite element model with the derived non-linear elastic properties and the measured displacements as boundary conditions. The critical strain energy release rate was constant with crack length ($118 \pm 14 \text{ J m}^{-2}$) and equivalent to a fracture toughness of $1.13 \pm 0.07 \text{ MPa m}^{1/2}$.

1. Introduction

Nuclear graphite is a key structural material in high temperature gas reactors (HTGR) because of its good neutron moderation, high temperature resistance and excellent radiation resistance [1,2]. Acting as a structural component that provides channels for the coolant, fuel, control rods and shutdown devices [3,4], nuclear graphite must sustain various possible loads and actions, such as self-weight, mechanical forces, thermal and radiation stresses and seismic actions [5] that may be sufficient to initiate fracture [6–9]. The fracture properties of graphite must therefore be considered in the design process to predict failure and ensure safe operation [10–13].

* Corresponding authors at: Research Center of Space Structures, Guizhou University, Guizhou, Guiyang 550025, China (H. Chen).

E-mail addresses: hqchen@gzu.edu.cn (H. Chen), james.marrow@materials.ox.ac.uk (T.J. Marrow).

Limitations on obtaining irradiated graphite material, such as extraction (e.g. trepanning) from a working reactor or irradiation in a material test reactor, restrict both the quantity and dimensions of graphite samples [5,14]. Thus, the fracture properties of irradiated graphite should be obtained from specimens that are small compared to the large standard specimens that can be used to assess unirradiated graphite [15,16].

The double cleavage drilled compression (DCDC) specimen geometry [17] has been used to investigate the fracture resistance of both irradiated and unirradiated graphite [18]. The DCDC specimen is a centimeter scale cuboid with a notched through-thickness hole, firstly used by Janssen [19] to study the fracture properties of glass. In the DCDC specimen, due to the Poisson effect, the applied longitudinal compression induces a transverse tensile stress that can drive the initiation and stable propagation of cracks that split the specimen. The critical stress intensity factor (i.e. fracture toughness) for quasi-static propagation of cracks with known dimensions can be obtained directly using a linear elastic analytical solution with knowledge of the critical load [20,21]. However, for small specimens, the analytical solutions have limitations since the assumed boundary conditions may not be satisfied due to frictional and constraint effects, and also possible misalignments and residual stresses [22,23]. To reliably evaluate the fracture toughness of small specimens, it is preferable to use experimental measurements of the boundary conditions rather than their assumed state.

The fracture toughness can be evaluated from full-field displacements, which can be measured locally to the crack by various techniques, using field fitting [24] and J-integral calculation [25]. Both of these local approaches have advantages over analytical solutions as they do not require knowledge of the loading conditions or specimen geometry [26]. For the field fitting approach, the critical stress intensity factor is determined by optimizing theoretical displacement fields, such as the linear elastic Williams' solution [27], to achieve the best fit with the measured displacements surrounding the crack [24,28]. However, this may not be accurate for quasi-brittle materials that develop a microcracked fracture process zone as a linear-elastic field may not exist close to the crack tip (i.e., tension softening) [22,29], and it is also difficult to determine the accurate position of the crack tip that is required for field fitting [24,25]. The J-integral method is applicable to linear elastic and non-linear materials and it is also less sensitive to the precise crack tip location [30–32]. Evaluated from the stress and strain fields surrounding a quasi-statically propagating crack tip, the J-integral is equivalent to the critical elastic strain energy release rate, G , which is the fracture toughness [33]. Li et al. developed a volume integral expression for the J-integral, known as the virtual crack extension method [34], which has better accuracy than the surface integral expression [30]. However, convergence of the volume integral contour is hindered by noise in the measured displacement fields [35]. One method, which makes the calculation of the J-integral more robust, imports the displacements measured at some distance from the crack tip as boundary conditions into a finite element model (FEM) [22,25,26,35,36] to then compute the censored displacements closer to the crack [25,35,37].

Accurate knowledge of the material's stress/strain relationship is essential to calculate the strain energy release rate using the J-integral method. In previous studies of the coarse-grained graphite (Gilsocarbon) for which the Young modulus is quite non-linear with strain in the unirradiated condition [29], the strain energy release rate was correctly derived from the displacement fields after calibration of the non-linear stress/strain relationship via an independent experiment [22]. Fine-grained graphite exhibits a lesser degree of nonlinearity [38] than coarse-grained graphite, but if linear elasticity is assumed there is still a significant overestimation of the crack tip strain energy and fracture toughness [39,40]. The irradiation and oxidation that can occur during graphite service in nuclear reactors can change both the Young modulus and the linearity of its stress–strain relationship [41–43]. This relationship can be measured by testing material that has experienced the same history in the reactor as the fracture specimen, but this may be constrained by its limited availability. Furthermore, small specimens may be affected by the significant spatial heterogeneity of properties in bulk graphite [44–47], so independent samples of material with the same history might not necessarily have the same properties. Ideally, the stress/strain relationship should be obtained in the same specimen that is used for the fracture test [39], but its evaluation is complicated for non-uniform stress states and non-linear properties. In this situation, the material constitutive parameters might be obtained by the inverse method of Finite Element Model Updating (FEMU), where the material parameters in a finite element model of the experimental test are updated iteratively to minimize the difference between the measured and FEM-calculated data until optimal values are determined [48,49]. The FEMU approach has been used successfully to characterize the non-linear properties of fine-grained (IG11) graphite under different stress states [38,48]. The FEMU approach has not previously been applied in fracture studies of graphite.

Some previous investigations on the fracture of nuclear graphite used surface displacement measurements by Digital Image Correlation (DIC) [50,51] or electronic speckle pattern interferometry (ESPI) [52,53]. However, crack propagation is not confined to the specimen surface. Digital Image Volume Correlation (DVC) is a three-dimensional full-field displacement measurement method [15,39,54], which can be applied to X-ray computed tomographs (XCT) that have sufficient speckle due to the heterogeneous attenuation contrast of the microstructure (i.e. porosity) [36,55,56]. Combined XCT/DVC is a powerful approach to visualize crack development and quantify specimen deformation in nuclear graphite, as it can provide knowledge of the 3D geometry of the crack front, the crack path and the crack opening angle [15,40].

The objective of this paper was to develop a method to simultaneously estimate the tensile softening behaviour of the Young modulus and the critical strain energy release rate in single small test specimen of graphite without prior knowledge of its constitutive properties. In situ laboratory XCT was applied to observe the fracture of a DCDC specimen made of a fine-grained graphite (SNG742). The three-dimensional displacements were measured by DVC and the strain softening relationship of the Young modulus was determined using the inverse FEMU method with the Nelder-Mead simplex optimization algorithm. A crack identification method, based on the variance of a wavelet transform, was developed to obtain the 3D crack shape from the measured displacement fields. Using the measured local displacement fields as boundary conditions and considering both linear and non-linear elastic properties, the strain energy release rate of the propagating crack was then determined by the volume integral method. The technical route of the method is summarized in Fig. 1.

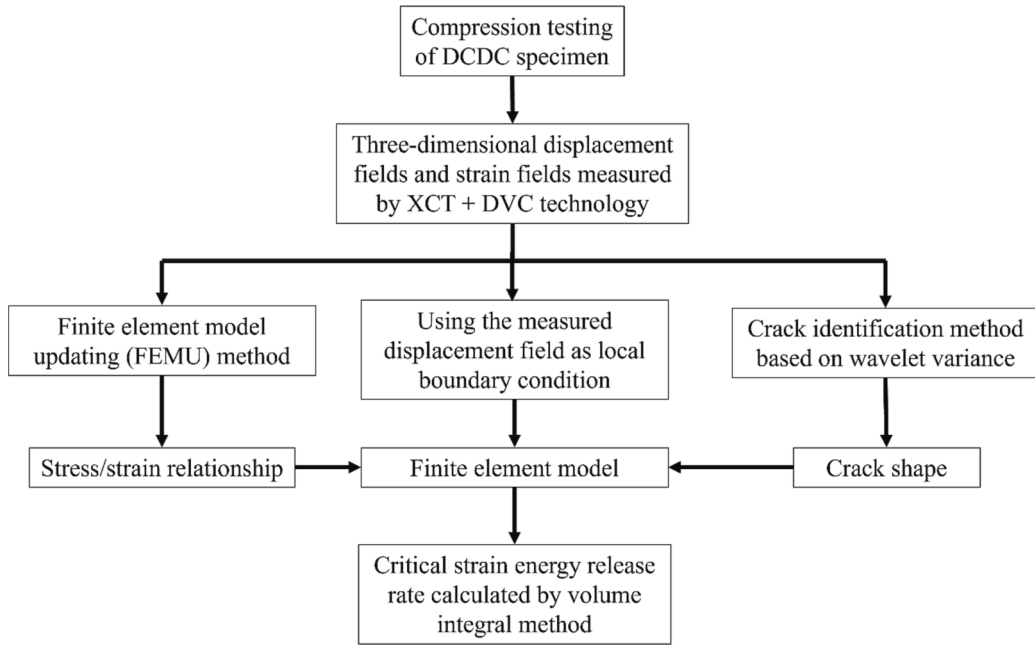


Fig. 1. The technical route to estimate the critical energy release rate.

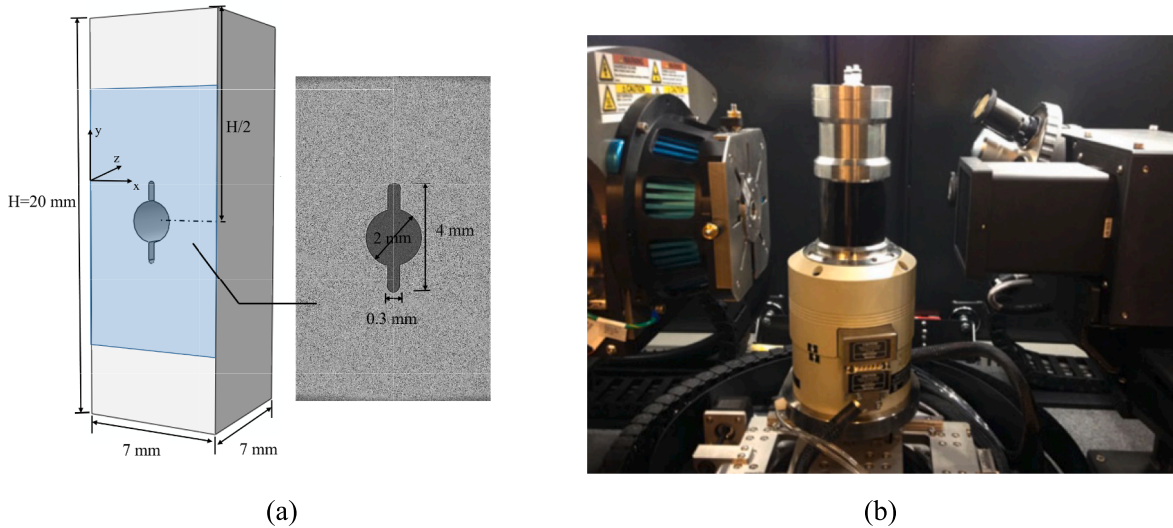


Fig. 2. (a) Geometric dimensions of DCDC specimen and an example XCT image (2D slice of 3D reconstruction); (b) Experimental setup with the Deben CT5000 loading rig (centre) between the X-ray source (left) and detector (right).

2. Experiments and analysis methods

2.1. Materials and experimental setup

SNG742, produced by Sinosteel Ltd. (Beijing, China), is a candidate graphite for next generation nuclear reactors [57] with a fine grain size (coke size $\sim 20 \mu\text{m}$) and density of 1.83 g/cm^3 . The geometry of the DCDC specimen ($X \times Y \times Z$) was $7 \times 20 \times 7 \text{ mm}$. A through-thickness central hole (2 mm diameter) aligned with the Z-direction was drilled with a central axial notch of 1 mm length and 0.5 mm width extending above and below the hole (Fig. 2a). Uniaxial compression loading was applied to the specimen using a 5 kN Deben CT5000 H250 rig with an X-ray transparent glassy carbon load-bearing tube, which was installed in a Zeiss Xradia 510 Versa X-ray microscope for in situ observation (Fig. 2b). Critical loading stages, based on preliminary tests, were selected to obtain tomographs at the preload ($\sim 20 \text{ N}$), 1116 N, 2000 N, 2050 N and 2080 N. Each tomograph was obtained using the operating parameters in Table 1.

Table 1
XCT operating parameters.

Operating Parameter	Value
Number of projections over 360° rotation	1601
Projection Field of view	~11.7 mm × 11.7 mm
Projection size	2008 × 2020 pixels
Voxel size	5.81 μm
Exposure time per projection	40 s
Energy	60 kV
Power	5 W

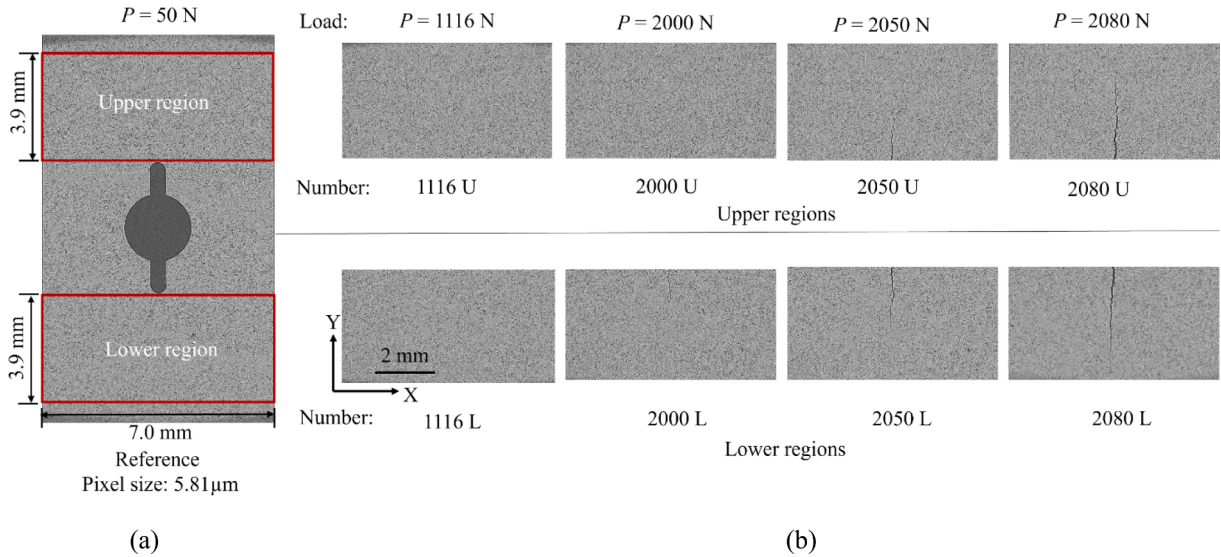


Fig. 3. (a) Tomographs cropped into upper regions and lower regions; (b) Vertical sections of tomographs corresponding to the loads of the in situ observations.

The tomographic images were reconstructed by the Zeiss' Scout-and-Scan software. No crack was observed at 1116 N, and cracks were only observed at 2000 N and above (Fig. 3).

2.2. Digital volume correlation (DVC)

The DVC analyses were conducted in the LaVision DaVis software (version 8.4.0) with the pre-load tomograph (~20 N) as the reference, using an initial FFT (Fast Fourier Transform) correlation then a series of multi-pass direct correlations of decreasing subset size. The analyses were applied separately to cropped upper and lower regions of the tomographs (Fig. 3a). These regions had dimensions ($X \times Y \times Z$) of $1200 \times 664 \times 1144$ voxels ($6.97 \times 3.86 \times 6.65$ mm) and their data are identified according to the corresponding load of the in situ observation and region (U for upper region and L for lower region) (Fig. 3b). Separate DVC analyses were performed using final subset sizes of $64 \times 64 \times 64$ voxels and $24 \times 24 \times 24$ voxels, both at 75 % overlap. In each case, the DVC analysis used four passes with a starting subset size of $192 \times 192 \times 192$ voxels and $96 \times 96 \times 96$ voxels respectively, also with 75 % overlap. Before each DVC analysis, the tomographs were manually registered (integer voxel precision) to remove large rigid body motions. The correlation was good with values close to 1 in all cases. The precision of DVC analysis tends to decrease with smaller subset size. The large subset size (dimension 64 voxels, ~370 μm) was used to obtain the softening relationship of Young modulus and critical energy release rate of the graphite, while the smaller subset size (dimension 24 voxels, ~140 μm) was used to identify the crack geometry due to the higher grid resolution of the DVC results.

2.3. Determination of softening relationship of Young modulus

(1) The FEMU inverse method

The Finite Element Model Updating (FEMU) inverse method was used to obtain the constitutive relationship of SNG742 graphite from the measured local deformations of the DCDC specimen in the uncracked state (1116U and 1116L in Fig. 3). The FEMU method establishes a FEM of the test specimen and iteratively updates the constitutive parameters to minimize the difference between the

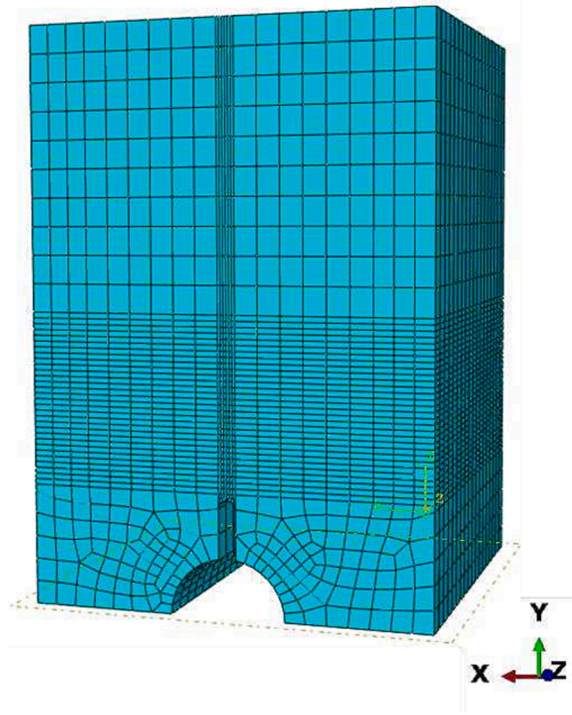


Fig. 4. Half model of the specimen.

measured strain fields and the values calculated by the FEM. The specific procedures were as follows:

Step 1: Establish a 3D FEM in Abaqus 6.14 with the same boundary conditions with the DCDC specimen in the test

In the FEM, considering symmetry, only half (upper side) of the specimen has been modeled to save computing time. The lower end of the specimen is constrained in the y direction and the upper end is subjected to a uniform compressive load of 1116 N. The Poisson ratio used in the model was 0.2 and was constant with strain. The SNG742 manufacturer datasheet provides a Poisson ratio of 0.2, which is typical for fine-grained graphite and graphites in general - in situ tensile tests of Gilsocarbon graphite showed the ratio of the average transverse bulk strain to the average axial bulk strain was approximately constant of 0.2 ± 0.03 [2]. Hexahedral solid elements are used and a region with refined mesh was created to match both the upper and lower regions with the DVC results. The finite element mesh is shown in Fig. 4.

Step 2: Embed a hypothetical constitutive relationship into the finite element model by a UMAT

The softening behaviour of the Young modulus in graphite with tension has been observed in several studies [29,38,48,58] and is essentially due to mechanical damage. The non-linear behaviour in compression is relatively weak [48,58]. The expression chosen to describe the reduction of Young modulus with increase of the maximum principal strain is given in Eq. (1):

$$E = (1 - d\epsilon_1)E_0 \quad (1)$$

where d is the softening parameter, ϵ_1 is the maximum principal strain, and the E_0 and E denote the undamaged and damaged Young modulus respectively. The parameters E_0 and d are set to initial values before optimization in the FEMU.

Step 3: Establish an objective function

The objective function is based on the squared difference between the strains measured by the DVC and the strains calculated by the FEM. It is expressed in Eq. (2):

$$Q(E_0, d) = \sum_{i=1}^N \left[(\epsilon_1^{FEM}(E_0, d) - \epsilon_1^{DVC})^2 \right]_i \quad (2)$$

where N represents the number of elements in the target region, ϵ_1^{FEM} denotes the maximum principal strain calculated by the FEM, and ϵ_1^{DVC} is the maximum principal strain at the positions of the FEM element integral points, which can be obtained by linear interpolation of the DVC strain field.

Step 4: Iteratively search for the optimal values of E_0 and d to minimize the objective function

This was done using the Nelder-Mead simplex algorithm, which is a classical direct search optimization algorithm that is well suited to unconstrained optimization problems without gradient information [48]. The flowchart of the inverse method is shown in Fig. 5.

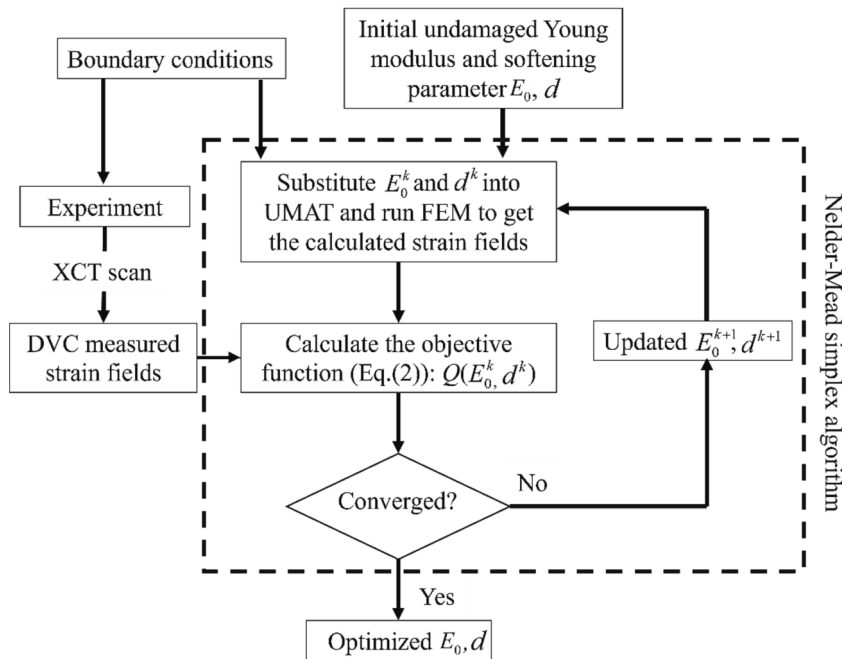


Fig. 5. Flowchart of the inverse method to determine the softening parameters of the Young modulus.

Table 2

Four sets of material parameters in the FEMs and the converged result using the inverse method.

No.	E_0 (MPa)	d	Initial E_0 (MPa)	Initial d	Converged E_0 (MPa)	Converged d
1	8000	100	15,000	0	7999.967	99.985
2	8000	140	15,000	0	7999.973	139.998
3	12,000	100	15,000	0	11999.886	99.994
4	12,000	140	15,000	0	12000.043	139.981

(2) Verification of the inverse method

Numerical simulations of the DCDC specimen were carried out to verify the accuracy and convergence of the inverse method. 'Experimental' strain fields were generated by 3D FEMs with four different sets of material parameters (see Table 2) for the undamaged Young modulus E_0 and the softening parameter d . The inverse FEMU method was then performed with the same initial material parameters (15,000 MPa and 0) and the 'experimental' maximum principal strain fields. The converged values of E and d are listed in Table 2, and agree very well with the true values of the FEM. Taking No.3 model as an example, the maximum principal strains in the specimen is shown in Fig. 6a, where the strains in the local region used for the inverse analysis range approximately from 0.0001 to 0.0015. The convergence of objective function (Eq. (2)) is shown in Fig. 6b. When the number of iterations exceeded 60, the errors between the numerical strains and DVC results were very small and the values of the objective function were all below 1×10^{-8} . The initial values affected the number of iterations but did not affect the final convergence results.

2.4. Crack characterisation

(1) Identification of the crack tip

Direct observation of the crack in the tomograph image can be difficult, so many studies identify the crack tip from the measured strain fields using a threshold of the opening strain [51,59,60] that is obtained from the local gradient of the crack opening displacements. The position of the crack tip determined in this way is quite sensitive to the chosen strain threshold [50], which is affected by the spatial resolution and precision of the image correlation analysis. A less subjective method is to use the phase congruency of the displacement field [15,36,61]. Lai developed a robust method for crack measurement that replaces the strain threshold with the threshold of the variance of the cross-correlation parameters, which significantly reduced the sensitivity of the threshold [50]; this method required the direction of crack propagation to be pre-determined.

An edge detection algorithm based on wavelet modulus maxima [39] can also be used to identify the crack path and determine the crack tip positions. This requires a wavelet threshold to be chosen, and in this study a wavelet variation (WV) method for crack tip

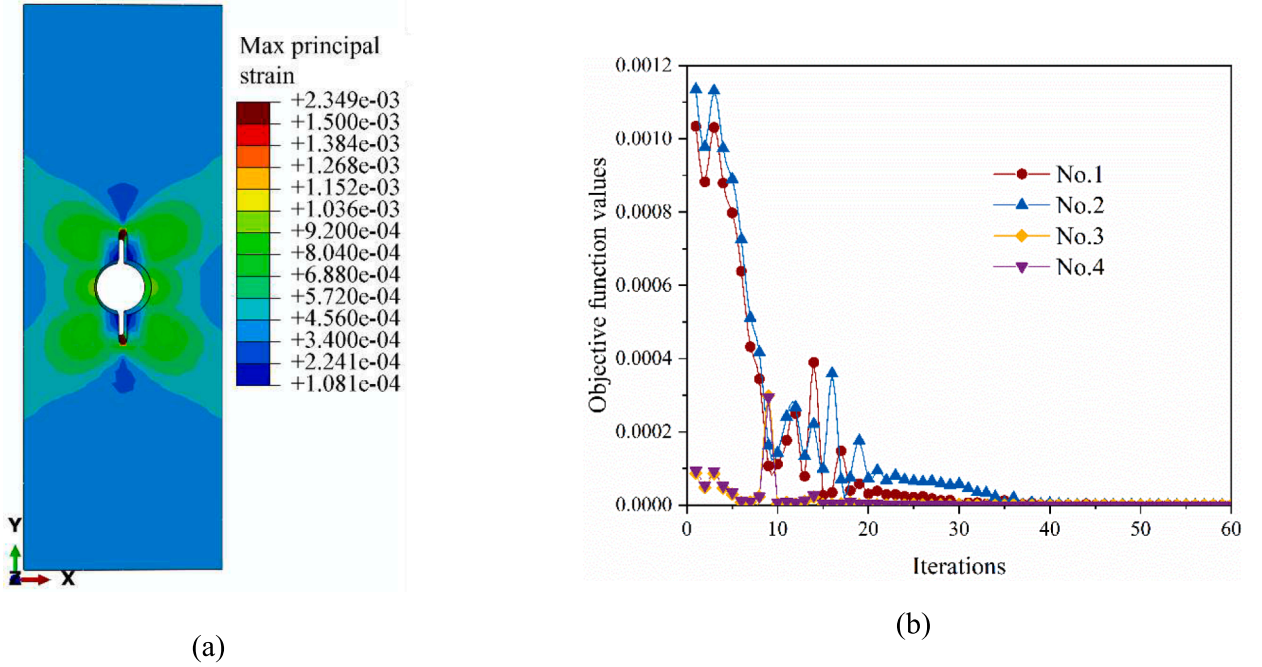


Fig. 6. (a) The maximum principal strains (example for model No.3); (b) Convergence of objective function with the number of iterations for each of the four models.

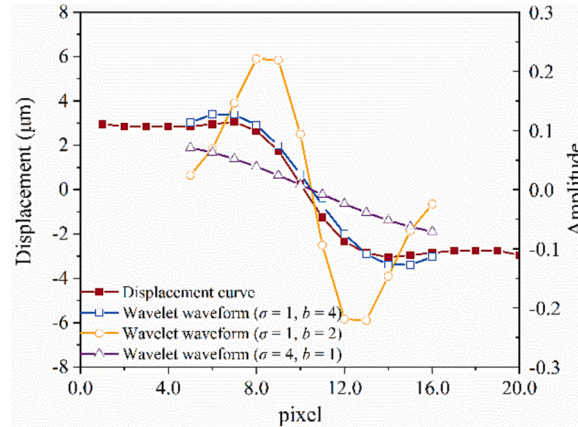


Fig. 7. The kernel functions for the wavelet transform with different parameters and the displacement curve caused by crack.

identification has been developed that does not require an arbitrary threshold choice. This method uses 2D image analysis, so the 3D displacement fields in the X direction (U_x) were considered as a series of X-Y plane slices to determine the positions of crack tips in each slice, and then the data from all the slices were combined to define the 3D crack. The analysis proceeded as follows, taking one 2D section as an example.

Firstly, a wavelet transform was applied to the U_x displacement fields. The first derivative of a bivariate Gaussian function with a scaling factor was used as the kernel function for the wavelet transform, as shown in Eqs. (3) and (4):

$$g_b(x, y) = \frac{1}{2\pi\sigma^2b} e^{-\left(\frac{x^2}{2\sigma^2} + \frac{y^2}{2\sigma^2}\right)} \quad (3)$$

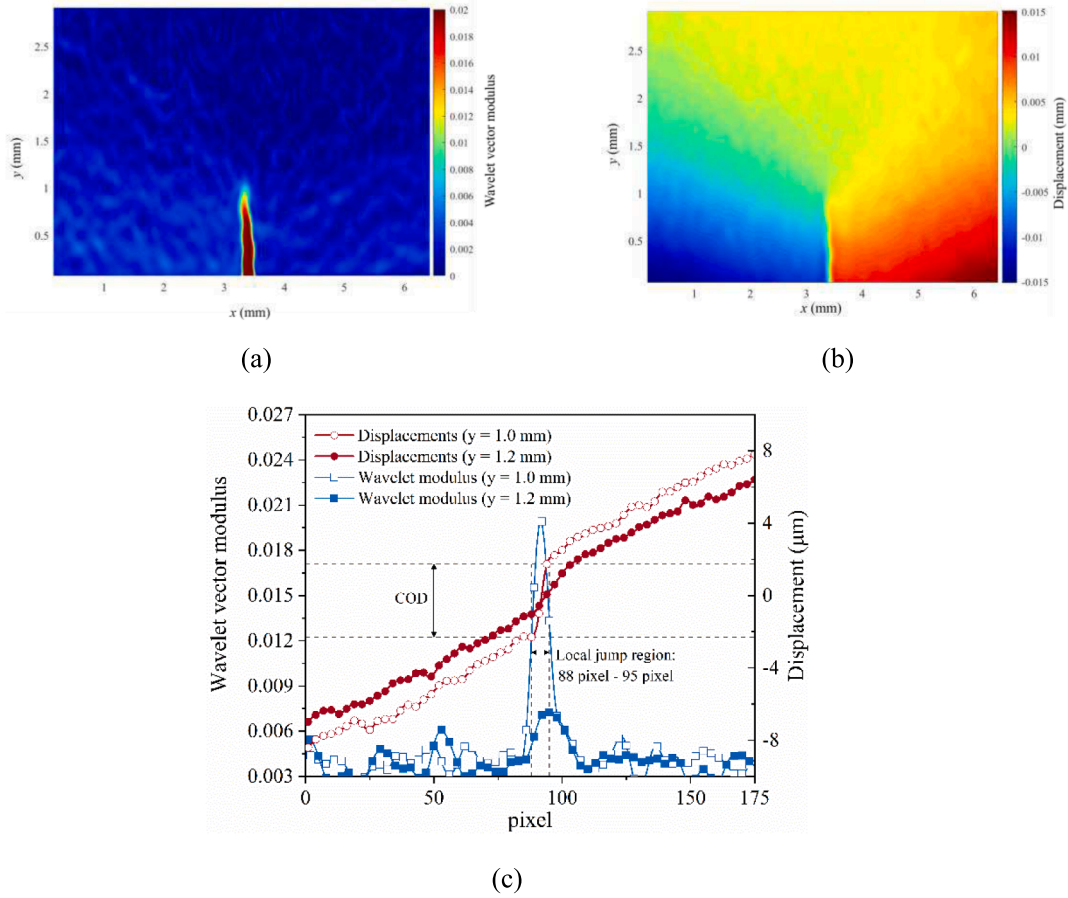


Fig. 8. Wavelet vector modulus and displacements in the 2000U region ($z = 0$ mm): (a) Wavelet vector modulus field; (b) X-direction displacement field measured by DVC; (c) Wavelet vector modulus and displacement profiles along the horizontal lines at $y = 1$ mm and $y = 1.2$ mm.

$$\begin{cases} \psi_x(x, y) = \frac{g_b(x, y)}{\partial x} = -\frac{x}{2\pi\sigma^4 b^2} e^{-\left(\frac{x^2}{b^2} + \frac{y^2}{\sigma^2}\right)} \\ \psi_y(x, y) = \frac{g_b(x, y)}{\partial y} = -\frac{y}{2\pi\sigma^4 b^2} e^{-\left(\frac{x^2}{b^2} + \frac{y^2}{\sigma^2}\right)} \end{cases} \quad (4)$$

where σ is the standard deviation of the Gaussian function, b is the scaling factor, and $g_b(x, y)$ is the Gaussian function with a scaling factor. σ and b affect the support region and amplitude of wavelet functions (Fig. 7). $\sigma = 1$, $b = 2$ and a kernel function size of 10×10 pixels were chosen to allow the wavelet function to correlate well with the displacement jump curve across the crack (Fig. 7).

The measured displacement field U_x in an X-Y slice of the DVC output was then considered as a digital image $f(x, y)$, and the wavelet transform was performed by calculating the convolution of the image $f(x, y)$ and wavelet function $\psi(x, y)$, as shown in Eqs. (5) and (6).

$$\begin{cases} W^x f(x, y) = b f(x, y) * \psi_x(x, y) \\ W^y f(x, y) = b f(x, y) * \psi_y(x, y) \end{cases} \quad (5)$$

$$|Wf(x, y)| = \sqrt{|W^x f(x, y)|^2 + |W^y f(x, y)|^2} \quad (6)$$

where $[W^x f(x, y), W^y f(x, y)]$ are wavelet transform vectors, and its modulus $|Wf(x, y)|$ can be calculated from the Eq. (6).

Taking the deformation measured in the 2000U region as an example, contours of the wavelet vector modulus and displacements are shown in Fig. 8. The wavelet modulus has a significant value at the displacement discontinuity that is caused by the crack opening. For comparison, the local displacement jumps caused by crack opening can be manually examined. As shown in Fig. 8c, the displacement profile at $y = 1$ mm clearly shows crack opening (high gradient and high wavelet modulus) while that at $y = 1.2$ mm does not (low gradient and low wavelet modulus). However, although the wavelet modulus increases with the displacement gradient across the crack, the selection of a constant threshold of displacement gradient to uniquely identify the crack tip position is still subjective.

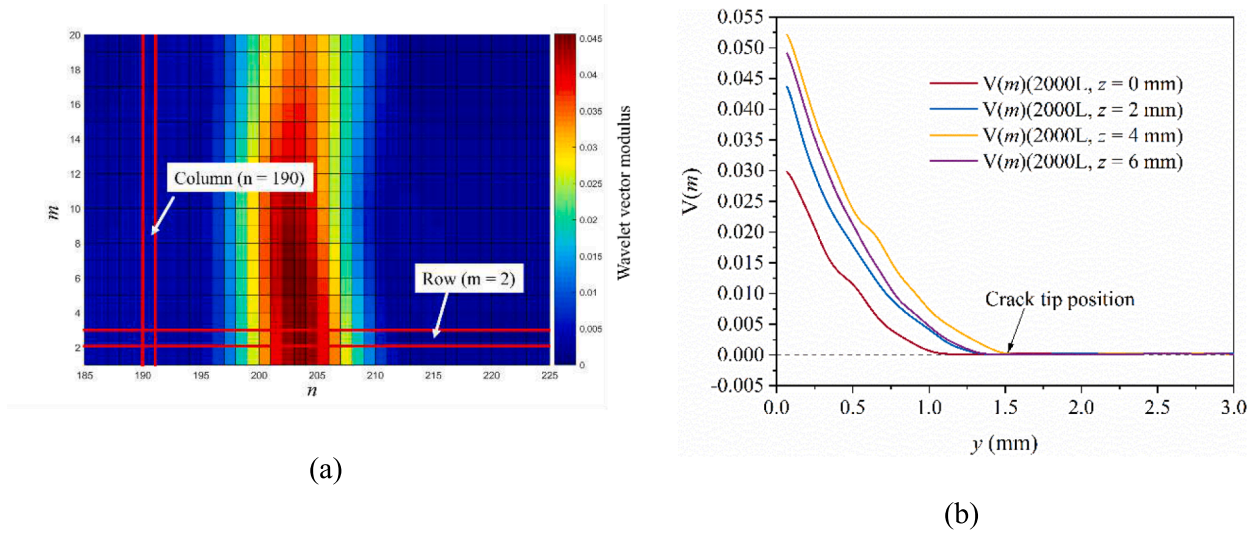


Fig. 9. The variance of wavelet vector modulus: (a) The rows and columns of the wavelet modulus matrix; (b) the variance of the wavelet vector modulus with y positions.

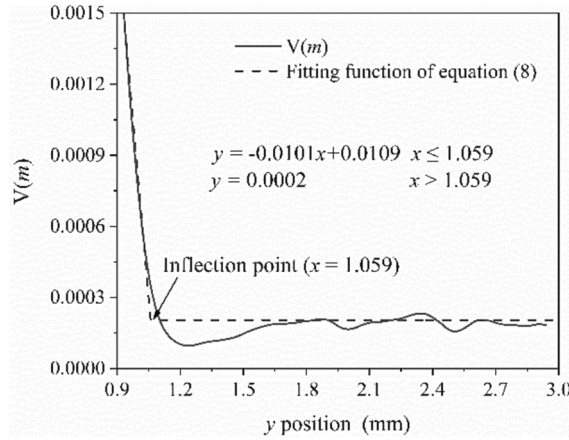


Fig. 10. Local $V(m)$ curve and its fitted piece-wise function.

To address this issue, the variances of the wavelet vector modulus were used. Fig. 8c shows that the variance of wavelet vector modulus at $y = 1$ mm is significantly (614 %) greater than that at $y = 1.2$ mm. The Wavelet vector modulus can be mapped as a matrix $V(m)$ that is given by Eq. (7)

$$V(m) = \left[\sum_{n=1}^N (|Wf(n, m)| - \sum_{n=1}^N |Wf(n, m)|/N)^2 \right] / N \quad (7)$$

where M and N represent the dimensions of matrix respectively. A schematic diagram of the wavelet modulus matrix is shown in the Fig. 9a and variations of the $V(m)$ along the y -axis are plotted in Fig. 9b. The values of $V(m)$ at the crack are significant, and elsewhere are close to 0.

The inflection point of the $V(m)$ profiles along the x -axis, as shown in Fig. 10, was determined by fitting the $V(m)$ profile with a piecewise function composed of a linear and a constant function, given in Eq. (8)

$$\begin{cases} y = bx + cx \leq a \\ y = ba + cx > a \end{cases} \quad (8)$$

where a , b , and c are fitting parameters optimized using nonlinear least squares method in MATLAB. From Fig. 10, it can be seen that $V(m)$ can be well fitted by the piecewise function, and the value of a provides an objective determination of the position of the crack tip.

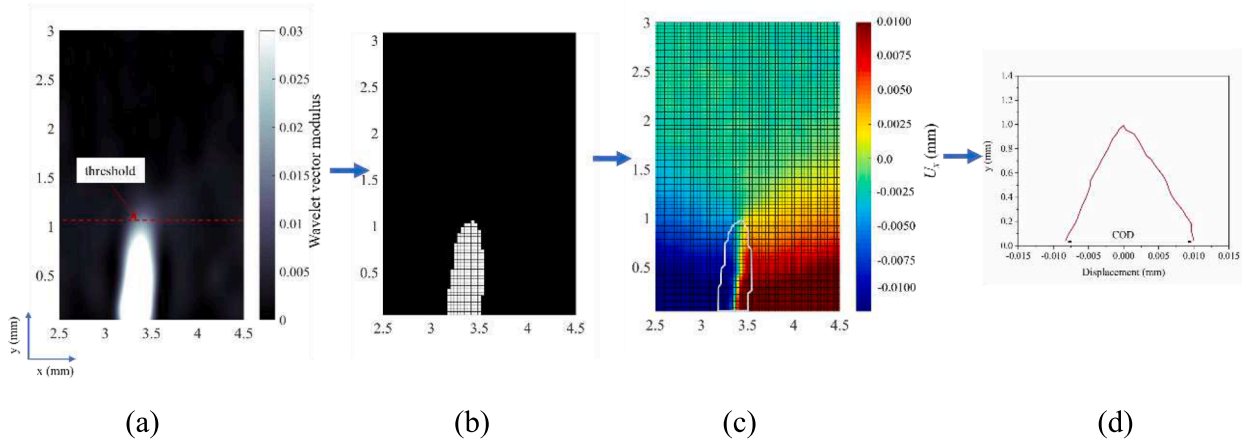


Fig. 11. The procedure to determine the COD: (a) thresholding of the wavelet modulus fields; (b) binary image containing crack and uncracked regions; (c) crack edges (white line); (d) COD calculated from the displacement difference between the crack edges.

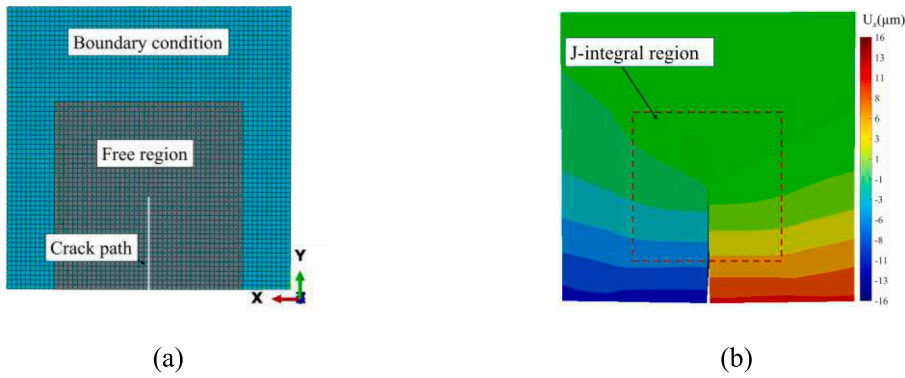


Fig. 12. Finite element analysis using the local DVC measured displacement field as boundary conditions: (a) Finite element model with crack and regions defined; (b) Displacement fields and J-integral contour on an X-Y plane ($z = 0$ mm).

(2) Identification of crack opening displacement (COD)

Generally, the COD can be obtained by measuring the displacement difference between both sides of the crack at a constant distance from the crack edge, but this may be an overestimate as the measurement can include elastic deformation [62]. The measurement distance should be as close as possible to the crack edges to reduce the errors.

The procedure for determining the COD in this study are shown in Fig. 11. The threshold of wavelet modulus that distinguished the crack in the wavelet modulus field was first determined, and the wavelet modulus field was converted into a binary image to define the edges between the cracked and uncrack regions according to this threshold. The difference between the U_x displacements on opposing edges of this region is the COD; its variation as a function of position y also gave the crack opening angle and confirmed the crack tip position.

2.5. Evaluation of strain energy release rate J

The strain energy release rates, J , were calculated numerically by evaluating the J-integral in a FEM that simulated a section of the specimen using the local boundary conditions at the cracked stages ($P = 2000$ N, 2050 N and 2080 N). Both cracked regions (upper region and lower region shown in Fig. 3a) of the specimen were studied. To reduce the computing time, a model size of ($X \times Y \times Z$) $3 \times 3 \times 6.7$ mm and mesh size of 0.05 mm were employed in the FE simulations (Fig. 12a). The model was divided into two regions: the boundary condition (BC) region and a free region where no nodal displacements were imposed and the crack was a free surface. In the BC region, the full-field displacements of DVC analysis obtained for the subset size of $64 \times 64 \times 64$ voxels were assigned to the nodes as boundary conditions (linear interpolation was used to obtain nodal displacements where there were no data). The displacements and strains in the free region around the crack were calculated by the FEM (Fig. 12b). Both linear elastic and non-linear elastic material properties were compared in the simulations. The non-linear elastic relationship was determined by the FEMU method in Section 2.3 and implemented as an Abaqus UMAT (User-defined MATERIAL law). The linear elastic analysis used a constant value that was the same

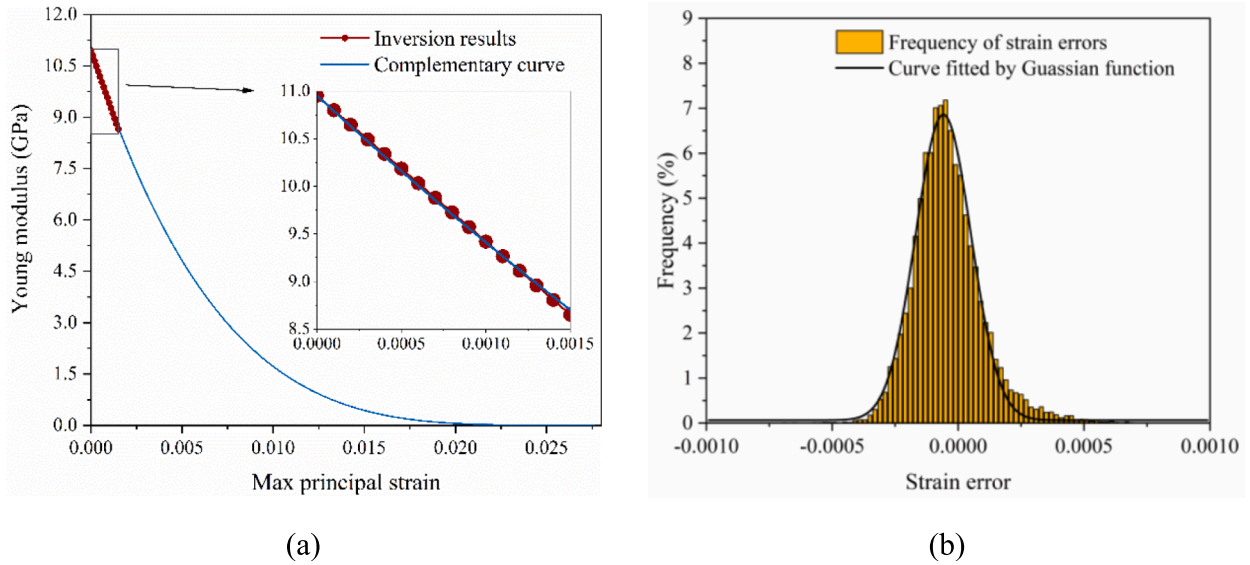


Fig. 13. The softening relationship of Young modulus and the distribution of strain errors: (a) tension softening curve of Young modulus (fitted data from inverse analysis and extrapolation); (b) Distribution frequency of the errors between the calculated strain by the optimized FEM and the measured strain.

Table 3

Crack lengths identified using different methods.

Load and region	Average crack length (WV method) (mm)	Average crack length (XCT image) (mm)	Error (%)
2000U	1.35 ± 0.13	1.31 ± 0.14	3.05
2000L	1.17 ± 0.09	1.15 ± 0.08	1.74
2050U	2.23 ± 0.10	2.15 ± 0.11	3.72
2050L	2.19 ± 0.09	2.16 ± 0.14	1.39
2080U	3.45 ± 0.08	3.41 ± 0.12	1.17
2080L	3.44 ± 0.06	3.36 ± 0.09	2.38
Average error			2.24

as the initial modulus of the non-linear elastic relationship, specifically E_0 in Eq. (1). The calculated stress and strain fields allowed evaluation of J along the crack tip by the virtual crack extension/domain integral method that is natively implemented in the Abaqus software [63].

3. Results and discussion

3.1. Tensile softening of the Young modulus

The softening relationship (red line with circle in Fig. 13a) of the Young modulus was inversely estimated from the maximum principal strain fields measured in the 1116U and 1116L regions using FEMU method. The results of the two regions were combined in one objective function to obtain one set of the constitutive parameters. The undamaged Young modulus E_0 and the softening parameter d , were determined to be 10.95 GPa and 140.05 respectively, which are close to $E_0 = 11$ GPa and $d = 120$ in another study on the IG11 fine-grained graphite [48]. The strain errors (difference between the maximum principal strains calculated by the optimized FEM and the measured strains) are shown as a frequency histogram in Fig. 13b. The distribution is approximately Gaussian with an expectation value close to 0 ($= -5.89 \times 10^{-5}$), and may reveal local displacement perturbations caused by microstructural inhomogeneities [64].

Due to the limited range of the maximum principal strains in the uncracked specimen, the inverse results can only describe modulus softening up to strains of ~ 0.0015 , which does not reach the strains developed near the crack tip in the subsequent observations. Therefore, the softening of the Young modulus was extrapolated using a model that assumed tensile strain induces microcracking that increases the porosity in proportion to the strain [15,22], as described by Eq. (9).

$$E = E_n(1 - (P_0 + A\varepsilon_1))^n \quad (9)$$

where P_0 is the initial porosity ($=0.12$) [57], $n = 4.12$ for interconnected pores of irregular shape [65], E_n is the Young's modulus of the non-porous graphite, and A is a constant. Fitting to the inversion curve (red line with circle in Fig. 13a), $E_n = 18.54$ GPa gives $E = 10.95$ GPa at zero strain and $A = 31.85$. This is close to the parameters obtained in a study of Gilsocarbon graphite [22] which found E_n

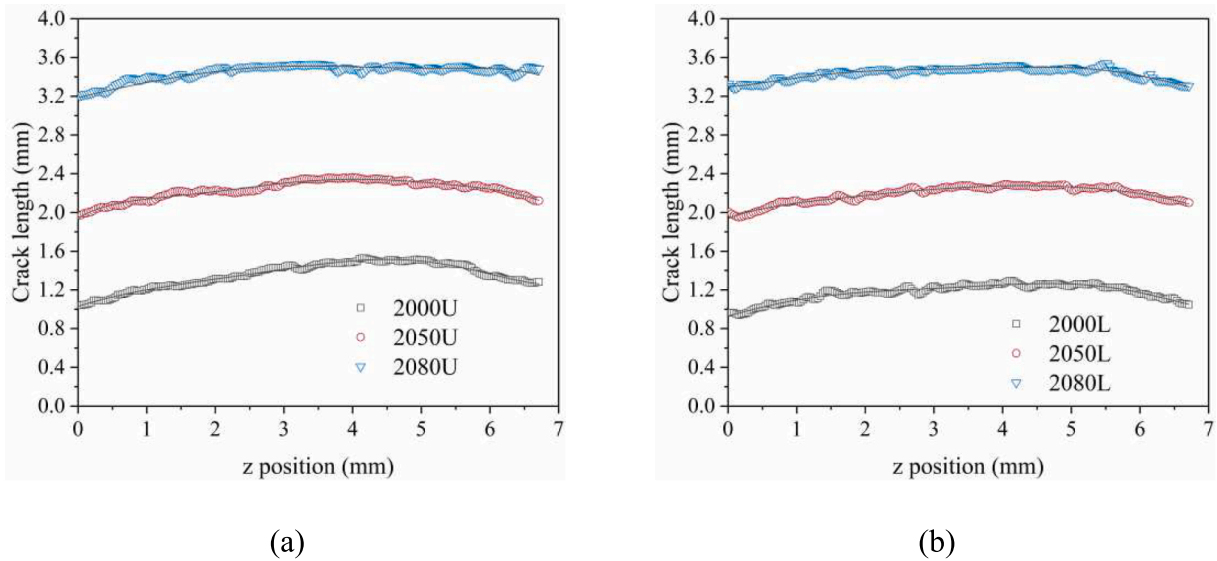


Fig. 14. The local crack lengths determined using the wavelet variance (WV) method: (a) Upper region; (b) Lower region.

= 23.84 GPa and $A = 36.34$ by fitting to tensile test data [29] for the change in Young modulus. These parameters were previously used to approximate the softening of SNG742 graphite [40].

3.2. Crack characterization

The crack tip position was determined from the DVC displacement fields using the wavelet variance (WV) method in section 2.4 and crack lengths were approximated as the distance from the pre-notch to the crack tip. The crack tip positions were also determined by manual inspection of the XCT images. The crack lengths, averaged through the thickness, are listed in Table 3 and there is very good agreement (average error about 2 %) between the WV method and inspection of the XCT images. The large standard deviations are an artefact of the curvature of the crack front (Fig. 14). The crack propagates with a similar shape (longer crack lengths near the centre) that may be due to uneven loading caused by geometric errors in the machining of the specimen. The J-integral is obtained from the boundary conditions along the crack front in the 3D finite element analysis [39], which is suited to curved cracks.

Mode I crack opening displacements (CODs) in the upper and the lower regions were obtained using the crack identification method introduced in section 2.4, as shown in Fig. 15a and Fig. 15b. The CODs at different load stages show geometrical similarity, and the relationship between the crack mouth opening displacement (CMOD) and crack length for all points along the crack front is shown in Fig. 15c. This can be well fitted by a quadratic equation (intercept at origin). The variation of crack length across the specimen width, calculated from the measured CMOD using this quadratic relation, agrees well with the observed crack lengths (see Fig. 15d). This suggests it may be possible to estimate the internal crack length from the CMOD observed at the surface, without the need for 3D observation.

The crack tip opening angle (CTOA) was obtained at three distances (0.1 mm, 0.2 mm and 0.3 mm) behind the crack tip (Fig. 15e). The average CTOA (approximately 2.19°) close to the crack tip is constant with the crack length, and is close to the 2° measured in a similar DCDC specimen of Gilsocarbon graphite [15]. The CTOA is connected to the crack strain field but may be affected by specimen geometry [40], so it might not be a reliable parameter to describe fracture resistance except in specimens of the same geometry. As shown in Fig. 15f, the COA and its standard deviation decrease with increasing distance from the crack tip and stabilize at $1.24^\circ \pm 0.06^\circ$. This suggests the COA might be suitable as a fracture parameter, if measured at a sufficient distance from the crack tip, which this approach may be used to establish.

3.3. Critical strain energy release rate J

The strain energy release rate J was evaluated from the J-integral in finite element simulations of the quasi-statically propagating crack, where the J-integral that is calculated in the free region converges readily due to the absence of displacement noise [35]. The J-integral is considered as the average of the plateau values within the free region, thus the strain energy release rate J was taken as the average of the second to nineteenth contours (Fig. 16a) – the first contour contains only the crack tip node and is neglected. The DCDC specimen gives stable mode I crack propagation [15,39], so this value of J represents the critical condition for mode-I fracture and is therefore a measure of the critical mode I strain energy release rate, J_{Ic} .

The values of J calculated from FEMs with linear elastic and non-linear elastic material models are shown in Fig. 16b and c respectively. The values are essentially constant over the thickness, which confirms the suitability of the FEM to consider a curved

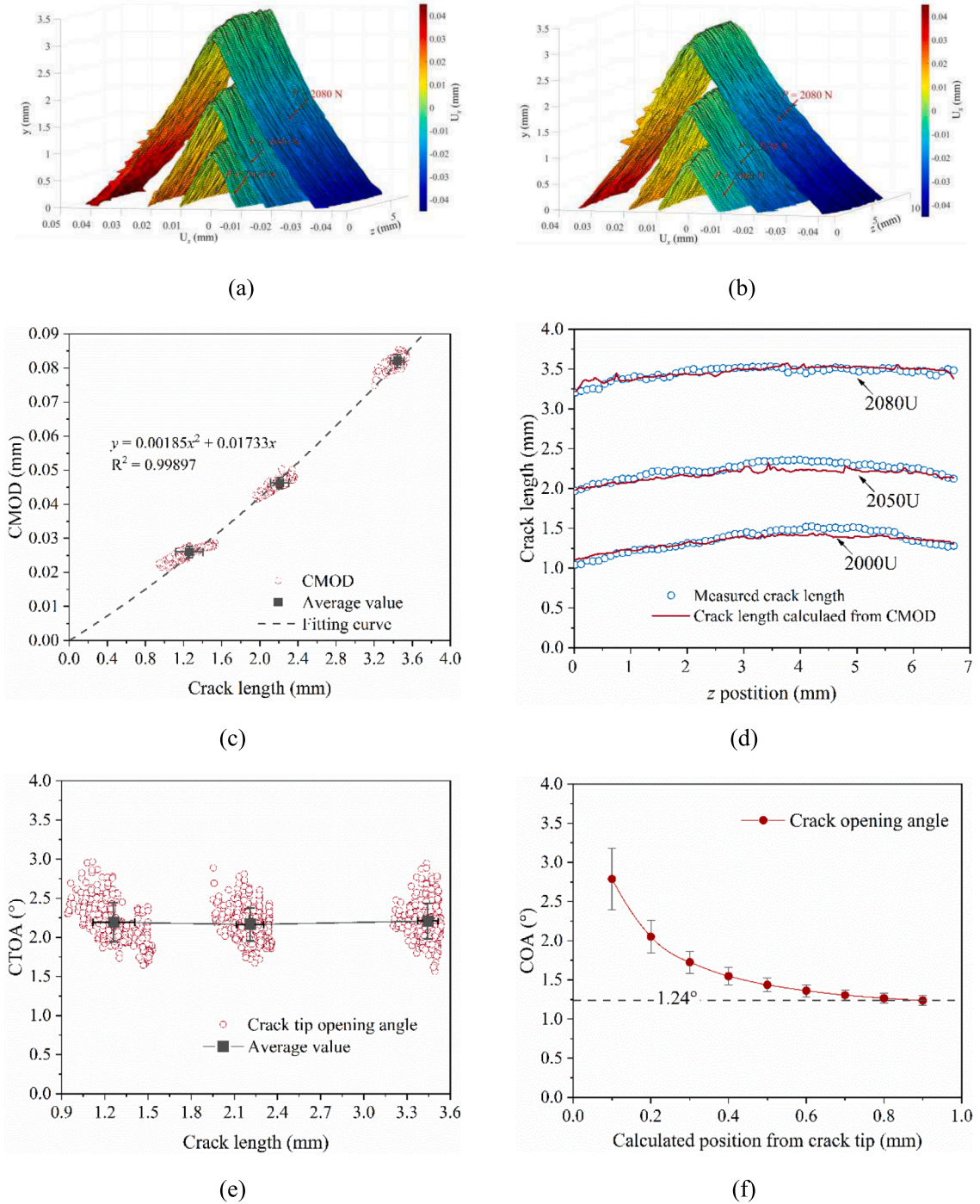
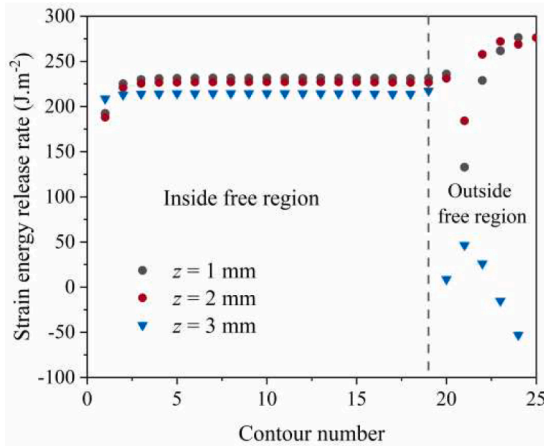


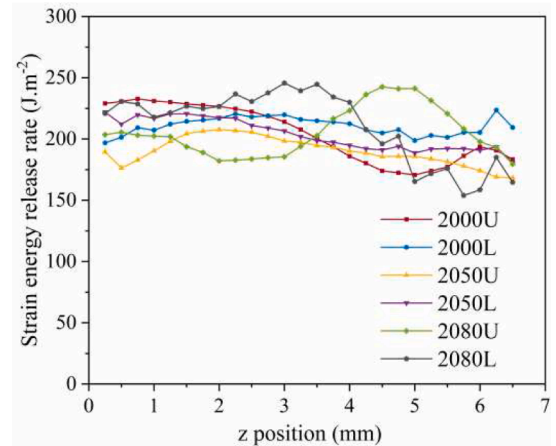
Fig. 15. Crack characterization: (a) 3D crack patterns in the upper region; (b) 3D crack patterns in the lower region; (c) local CMOD versus the crack lengths; (d) comparison of the local crack lengths calculated from the CMOD and the measured results; (e) CTOA versus crack length; (f) Average of the COA at different distances from the crack tip.

crack front [39]. The average J is $204.06 \pm 19.76 \text{ J m}^{-2}$ for the linear elastic model and $118.01 \pm 14.32 \text{ J m}^{-2}$ for the non-linear model. Compared to the linear elastic model, the value of J obtained from the non-linear model was reduced by 42 % (from 204 J m^{-2} to 118 J m^{-2}). This is slightly smaller than the 53 % difference reported for coarse-grained Gilsocarbon graphite [15] that may be due to its greater non-linearity [22].

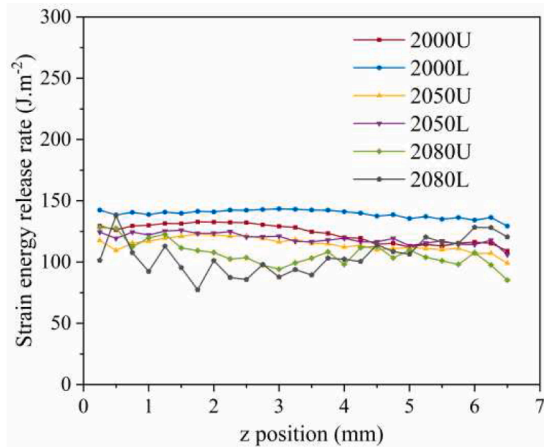
The variation of J with crack length is shown in Fig. 16d. There was no significant change in the J with increasing crack length, which is consistent with previous studies of this fine-grained graphite [40], although rising toughness with crack length (R-curve)



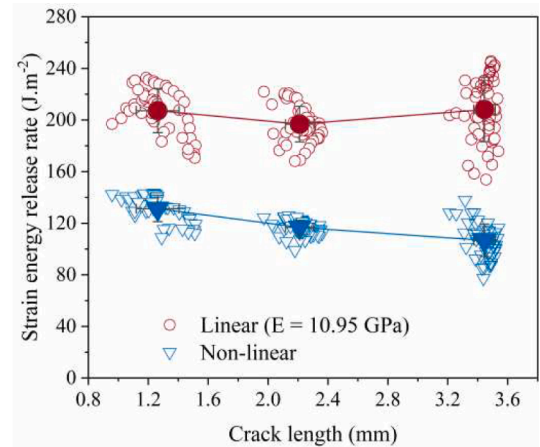
(a)



(b)



(c)



(d)

Fig. 16. The strain energy release rate calculation: (a) example of the J values with contour number at 3 positions along the crack front in 2000U region using the linear elastic model; (b) variation of J along the thickness direction (linear elastic model, $E = 10.95$ GPa); (c) variation of the J along the thickness direction (non-linear model); (d) The strain energy release rate versus crack length for linear and non-linear models.

behaviour has been reported in SNG742 for longer crack propagation over ~ 5 mm. R-curve behaviour has been reported in coarse-grained graphites for specimens with size of the order of several cm [51,66], however, the extent of crack growth in this study is insufficient to evolve significant toughening from mechanisms such as crack branching and bridging. The fluctuations in the R curve may be due to the heterogeneity of the material [67] and errors in identifying the crack tip positions [35] as the measurements are made over a small length scale.

As the loading of the crack in the DCDC specimen is mode I, an equivalent mode I stress intensity factor K may be obtained from J by using Eq. (10). For the non-linear elastic material, with the approximation that E has the value of the undamaged E_0 (10.95 GPa), the equivalent K is 1.13 ± 0.07 MPa $m^{1/2}$ and this is very close to the expected fracture toughness of SNG742 graphite of 1.12 MPa $m^{1/2}$ obtained in a standard large test specimen [68]. For the linear elastic material model, K is 1.49 ± 0.07 MPa $m^{1/2}$, which is an overestimate.

$$K = \sqrt{J^* E} \quad (10)$$

The effect of the non-linear tension softening material model on the maximum principal stress fields can be seen in the example for the 2000U region in a comparison with the linear model (Fig. 17). The maximum stress around the crack tip for the linear model is 101.5 MPa (much higher than the reported flexural strength 45 MPa of SNG742 graphite [57]), whereas in the non-linear elastic model it is 38 MPa. The strain fields of the two models are the same as they have the same displacement boundary conditions, but the higher stresses close to the crack tip in the linear elastic model result in a higher calculated strain energy release rate. Using a suitable non-

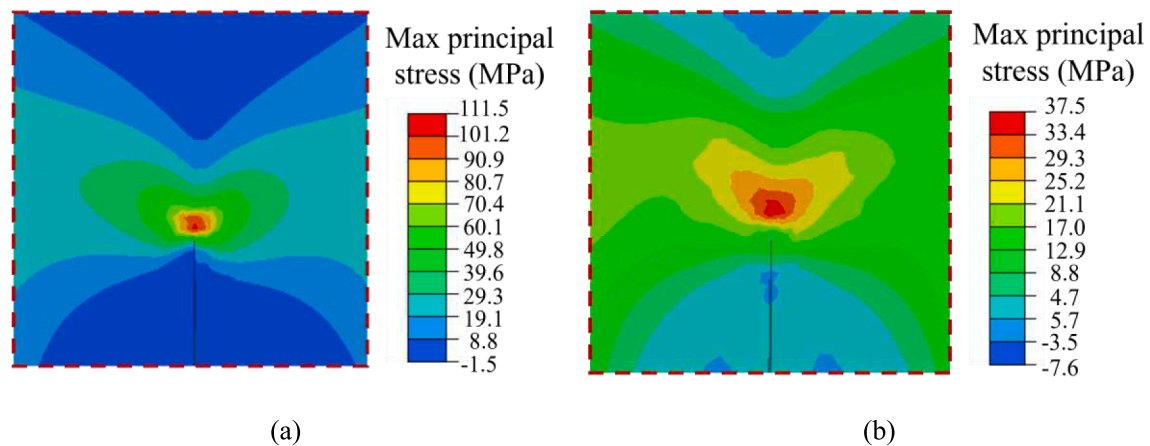


Fig. 17. Maximum principal stress fields used to evaluate the J-integral on X-Y plane ($z = 0$ mm): (a) linear elastic model; (b) non-linear elastic model.

linear constitutive relation for the graphite material, obtained via the FEMU analysis of the same specimen, gives more realistic stresses in the crack tip region where the J-integral is evaluated, and this provides a more accurate estimation of the strain energy release rate.

4. Conclusions

A fracture test of a SNG742 graphite specimen in the double cleavage drilled compression (DCDC) geometry has been observed in situ by X-ray computed tomography. 3D displacement fields within the specimen were obtained by digital volume correlation of the tomographs and are further used to estimate the softening relationship of Young modulus, the 3D crack geometry and the critical strain energy release rate for crack propagation.

The following may be concluded:

- (1) The Finite Element Model Update (FEMU) technique allows the inverse estimation of the non-linear (tension softening) stress/strain relationship by using the local displacement fields and applied loads of a small specimen test fracture test of graphite.
- (2) A Wavelet Variance (WV) method has been developed to provide an objective and reliable measurement of crack lengths and crack opening displacements.
- (3) With accurate crack information and nonlinear elastic material properties, a finite element (FE) analysis that used the measured displacements as boundary conditions estimated the strain energy release rate of SNG742 graphite to be $118 \pm 14 \text{ J m}^{-2}$, which agreed with the critical stress intensity factor that has been reported for standard large specimen tests of the same grade of graphite.

CRediT authorship contribution statement

Hongniao Chen: Writing – original draft, Software, Investigation, Funding acquisition. **Jie Shen:** Software, Methodology, Formal analysis. **Daniel Scotson:** Investigation, Formal analysis. **Xiaochao Jin:** Software, Investigation. **Houzheng Wu:** Resources. **T. James Marrow:** Conceptualization, Methodology, Supervision, Writing – review & editing.

Declaration of Competing Interest

The authors declare that they have no known competing financial interests or personal relationships that could have appeared to influence the work reported in this paper.

Data availability

Data will be made available on request.

Acknowledgement

The work was supported by the National Natural Science Foundation of China (Grant No. 52278251), Guizhou Provincial Sciences and Technology Projects (ZK[2022] Key 007), and the International Exchanges 2021 funded by the Royal Society (Ref: IEC\NSFC \211449). The graphite test specimens were kindly provided by Sinosteel. H.N. Chen acknowledges the support of the China

Scholarship Fund (Award No. 201906675001) that enabled her participation in this work at Oxford University. The X-ray microscope, software and workstation used for the tomography and digital volume correlation analysis was supported by EPSRC Grant EP/M02833X/1 “University of Oxford: experimental equipment upgrade”.

References

- [1] Kelly BT. Graphite—the most fascinating nuclear material. *Carbon* 1982;20(1):3–11.
- [2] Taylor R, Brown RG, Gilchrist K, Hall E, Hodds AT, Kelly BT, et al. The mechanical properties of reactor graphite. *Carbon* 1967;5(5):519–31.
- [3] Rose A, Tucker MO. A fracture criterion for nuclear graphite. *J Nucl Mater* 1982;110(2–3):186–95.
- [4] Moskovic R, Flewitt PEJ, Schlagen E, Smith G, Crocker AG, Hodgkins A, et al. Understanding fracture behaviour of PGA reactor core graphite: perspective. *Mater Sci Technol* 2014;30(2):129–45.
- [5] Carroll MC, Rohrbaugh DT, Chakraborty P, Swank WD. Evaluating alternate test techniques to characterize mechanical properties in nuclear-grade graphites. 8th International Topical Meeting on High Temperature Reactor Technology. Las Vegas, NV, United states: American Nuclear Society; 2016. p. 269–75.
- [6] Mohanty S, Majumdar S, Srinivasan M. Constitutive modeling and finite element procedure development for stress analysis of prismatic high temperature gas cooled reactor graphite core components. *Nucl Eng Des* 2013;260:145–54.
- [7] Sumita J, Shimazaki Y, Shibata T. Investigation on structural integrity of graphite component during high temperature 950 °C continuous operation of HTTR. *J Nucl Sci Technol* 2014;51(11–12):1364–72.
- [8] Tsang DKL, Marsden BJ. The development of a stress analysis code for nuclear graphite components in gas-cooled reactors. *J Nucl Mater* 2006;350(3):208–20.
- [9] Svalbonas V, Stilwell TC, Zudans Z. Rules for design of nuclear graphite core components — Some considerations and approaches. *Nucl Eng Des* 1978;46(2):313–33.
- [10] Hindley MP, Blaine DC, Groenwold AA, Becker TH. Failure prediction of full-size reactor components from tensile specimen data on NBG-18 nuclear graphite. *Nucl Eng Des* 2015;284:1–9.
- [11] Vreeling JA, Wouters O, Laan JGVD. Graphite irradiation testing for HTR technology at the High Flux Reactor in Petten. *J Nucl Mater* 2008;381(1):68–75.
- [12] Haag G, Mindermann D, Wilhelm G, Persicke H, Ulsamer W. Development of reactor graphite. *J Nucl Mater* 1990;171(1):41–8.
- [13] Yu S, Fang X, Wang H, Li C. Failure probability study of HTR graphite component using microstructure-based model. *Nucl Eng Des* 2012;253:192–9.
- [14] Tzelepi A, Ramsay P, Steer AG, Dinsdale-Potter J. Measuring the fracture properties of irradiated reactor core graphite. *J Nucl Mater* 2018;509:667–78.
- [15] Jin X, Wade-Zhu J, Chen Y, Mummery PM, Fan X, Marrow TJ. Assessment of the fracture toughness of neutron-irradiated nuclear graphite by 3D analysis of the crack displacement field. *Carbon* 2021;171:882–93.
- [16] Standard Test Method for Determination of Fracture Toughness of Graphite at Ambient Temperature. ASTM International; 2020.
- [17] Pallares G, Ponson L, Grimaldi A, George M, Prevot G, Ciccotti M. Crack opening profile in DCDC specimen. *Int J Fract* 2009;156(1):11–20.
- [18] Wade-Zhu J, Krishna R, Bodey AJ, Davies M, Bourne NK, Rau C, et al. 4D synchrotron X-ray microtomography of fracture in nuclear graphite after neutron irradiation and radiolytic oxidation. *Carbon* 2020;168:230–44.
- [19] Janssen C. Specimen for fracture mechanics studies on glass. *Revue de Physique Appliquée* 1977;12(5):803.
- [20] He MY, Turner MR, Evans AG. Analysis of the double cleavage drilled compression specimen for interface fracture energy measurements over a range of mode mixities. *Acta Metall Mater* 1995;43(9):3453–8.
- [21] Warren WE. Theoretical analysis of the double cleavage drilled compression specimen. *Int J Fract* 1987;33(3):223–35.
- [22] Barhli SM, Saucedo-Mora L, Jordan MSL, Cinar AF, Reinhard C, Mostafavi M, et al. Synchrotron X-ray characterization of crack strain fields in polygranular graphite. *Carbon* 2017;124:357–71.
- [23] Marrow J, Scotson D, Koko A, Jin X, Chen H, Chen Y, et al. Small-Specimen Testing, with Image-Based Analysis, for Crack Propagation Resistance in Polygranular Nuclear Graphite. Symposium on Graphite Testing for Nuclear Applications: The Validity and Extension of Test Methods for Material Exposed to Operating Reactor Environments: ASTM International; 2022. p. 1–17.
- [24] McNeill SR, Peters WH, Sutton MA. Estimation of stress intensity factor by digital image correlation. *Eng Fract Mech* 1987;28(1):101–12.
- [25] Barhli S. Advanced quantitative analysis of crack fields, observed by 2D and 3D image correlation, volume correlation and diffraction mapping: University of Oxford; 2017.
- [26] Koko A, Earp P, Wigger T, Tong J, Marrow TJ. J-integral analysis: An EDX and DIC comparative study for a fatigue crack. *Int J Fatigue* 2020;134:105474.
- [27] Williams ML. On the stress distribution at the base of a stationary crack. *J Appl Mech* 2021;24(1):109–14.
- [28] Abshirini M, Soltani N, Marashizadeh P. On the mode I fracture analysis of cracked Brazilian disc using a digital image correlation method. *Opt Lasers Eng* 2016;78:99–105.
- [29] Marrow TJ, Liu D, Barhli SM, Saucedo Mora L, Vertyagina Y, Collins DM, et al. In situ measurement of the strains within a mechanically loaded polygranular graphite. *Carbon* 2016;96:285–302.
- [30] Becker TH, Mostafavi M, Tait RB, Marrow TJ. An approach to calculate the J-integral by digital image correlation displacement field measurement. *Fatigue Fract Eng Mater Struct* 2012;35(10):971–84.
- [31] Ast J, Ghidelli M, Durst K, Göken M, Sebastiani M, Korsunsky AM. A review of experimental approaches to fracture toughness evaluation at the micro-scale. *Mater Des* 2019;173:107762.
- [32] Courtin S, Gardin C, Bézein G, Hamouda BH, H. Advantages of the J-integral approach for calculating stress intensity factors when using the commercial finite element software ABAQUS. *Eng Fract Mech* 2005;72(14):2174–85.
- [33] Rice JR. A path independent integral and the approximate analysis of strain concentration by notches and cracks. *J Appl Mech* 1968;35(2):379–86.
- [34] Li FZ, Shih CF, Needleman A. A comparison of methods for calculating energy release rates. *Eng Fract Mech* 1985;21(2):405–21.
- [35] Barhli SM, Mostafavi M, Cinar AF, Hollis D, Marrow TJ. J-integral calculation by finite element processing of measured full-field surface displacements. *Exp Mech* 2017;57(6):997–1009.
- [36] Koko A, Singh S, Barhli S, Connelley T, Vo NT, Wigger T, et al. 3-Dimensional analysis of fatigue crack fields and crack growth by in situ synchrotron X-ray tomography. *Int J Fatigue* 2023;170:107541.
- [37] Su X, Wan W, Dunne FP, Marrow TJ. Crack field analysis by optical DIC of short cracks in Zircaloy-4. *Procedia Struct Integrity* 2022;39:663–70.
- [38] Liu G, Wang L, Yi Y, Sun L, Shi L, Ma S. Inverse identification of graphite damage properties under complex stress states. *Mater Des* 2019;183:108135.
- [39] Shen J, Marrow TJ, Scotson D, Jin X, Wu H, Chen H. Combined evaluation of Young modulus and fracture toughness in small specimens of fine grained nuclear graphite using 3D image analysis. *J Nucl Mater* 2022;563:153642.
- [40] Jin X, Marrow TJ, Wang J, Chen Y, Chen H, Scotson D, et al. Crack propagation in fine grained graphites under mode I and mixed-mode loading, as observed in situ by microtomography. *Carbon* 2022;193:356–67.
- [41] Kelly BT, Burchell TD. Structure-related property changes in polycrystalline graphite under neutron irradiation. *Carbon* 1994;32(3):499–505.
- [42] Eason ED, Hall GN, Marsden BJ, Heys GB. A model of Young’s modulus for Gilsocarbon graphites irradiated in oxidising environments. *J Nucl Mater* 2013;436(1):201–7.
- [43] Kim ES, No HC, Kim BJ, Oh CH. Estimation of graphite density and mechanical strength variation of VHTR during air-ingress accident. *Nucl Eng Des* 2008;238(4):837–47.
- [44] Arai T, Sato S, Oku T, Schiffrers H, Delle W. Assessment of heterogeneity and anisotropy of IG-110 graphite for nuclear components. *J Nucl Sci Technol* 1991;28(8):713–20.
- [45] Arregui-Mena JD, Bodel W, Worth RN, Margetts L, Mummery PM. Spatial variability in the mechanical properties of Gilsocarbon. *Carbon* 2016;110:497–517.
- [46] Arregui-Mena JD, Margetts L, Griffiths DV, Lever L, Hall G, Mummery PM. Spatial variability in the coefficient of thermal expansion induces pre-service stresses in computer models of virgin Gilsocarbon bricks. *J Nucl Mater* 2015;465:793–804.

- [47] Metcalfe M, Tzelepi N, Wilde D. Effect of test specimen size on graphite strength. Graphite Testing for Nuclear Applications: The Significance of Test Specimen Volume and Geometry and the Statistical Significance of Test Specimen Population: ASTM International; 2014.
- [48] Liu G, Wang L, Yi Y, Sun L, Shi L, Jiang H, et al. Inverse identification of tensile and compressive damage properties of graphite material based on a single four-point bending test. *J Nucl Mater* 2018;509:445–53.
- [49] Avril S, Bonnet M, Bretelle A-S, Grédiac M, Hild F, Ienny P, et al. Overview of identification methods of mechanical parameters based on full-field measurements. *Exp Mech* 2008;48(4):381–402.
- [50] Lai S, Shi L, Fok A, Li H, Sun L, Zhang Z. A new method to measure crack extension in nuclear graphite based on digital image correlation. *Sci Technol Nucl Install* 2017;2017:1–10.
- [51] Becker TH, Marrow TJ, Tait RB. Damage, crack growth and fracture characteristics of nuclear grade graphite using the Double Torsion technique. *J Nucl Mater* 2011;414(1):32–43.
- [52] Chen HHN, Su RKL, Fok SL, Zhang HG. Fracture behavior of nuclear graphite under three-point bending tests. *Eng Fract Mech* 2017;186:143–57.
- [53] Su RKL, Chen HH, Fok SL, Li H, Singh G, Sun L, et al. Determination of the tension softening curve of nuclear graphites using the incremental displacement collocation method. *Carbon* 2013;57:65–78.
- [54] Mostafavi M, Vertyagina Y, Reinhard C, Bradley R, Jiang X, Galano M, et al. 3D studies of indentation by combined X-ray tomography and digital volume correlation. *Key Eng Mater* 2013;592–593:14–21.
- [55] Mostafavi M, Collins DM, Cai B, Bradley R, Atwood RC, Reinhard C, et al. Yield behavior beneath hardness indentations in ductile metals, measured by three-dimensional computed X-ray tomography and digital volume correlation. *Acta Mater* 2015;82:468–82.
- [56] De Souza MAM, Pardini LC, Botelho EC, Costa ML. X-ray tomography applied to the void/defect measurement of hybrid CFRC/SiC composites. *Mater Res Express* 2019;6(4):045606.
- [57] Lu W, Li X, Wu X, Sun L, Li Z. Investigation on the oxidation behavior and multi-step reaction mechanism of nuclear graphite SNG742. *J Nucl Sci Technol* 2019;57(3):263–75.
- [58] Liu D, Zillhardt T, Earp P, Kabra S, Connolly T, James MT. In situ measurement of elastic and total strains during ambient and high temperature deformation of a polygranular graphite. *Carbon* 2020;163:308–23.
- [59] Li H, Li J, Singh G, Fok A. Fracture behavior of nuclear graphite NBG-18. *Carbon* 2013;60:46–56.
- [60] Mostafavi M, Schmidt MJJ, Marsden BJ, Marrow TJ. Fracture behaviour of an anisotropic polygranular graphite (PGA). *Mater Sci Eng A Struct Mater* 2012;558:265–77.
- [61] Yan L, Cinar A, Ma S, Abel R, Hansen U, Marrow TJ. A method for fracture toughness measurement in trabecular bone using computed tomography, image correlation and finite element methods. *J Mech Behav Biomed Mater* 2020;109:103838.
- [62] Zhang J, Yu Z, Tang Y, Shen J, Chen H. Fracture properties of concrete under cyclic loading. *Constr Build Mater* 2021;281:122610.
- [63] Parks DM. The virtual crack extension method for nonlinear material behavior. *Comput Methods Appl Mech Eng* 1977;12(3):353–64.
- [64] Joyce MR, Marrow TJ. Microstructural scale strain localisation in nuclear graphite. *J Nucl Mater* 2008;381(1–2):171–6.
- [65] Vertyagina Y, Marrow TJ. A multi-scale three-dimensional Cellular Automata fracture model of radiolytically oxidised nuclear graphite. *Carbon* 2017;121:574–90.
- [66] Hodgkins A, Marrow TJ, Mummery P, Marsden B, Fok A. X-ray tomography observation of crack propagation in nuclear graphite. *Mater Sci Technol* 2006;22(9):1045–51.
- [67] Yoon JH, Byun TS, Strizak JP, Snead LL. Characterization of tensile strength and fracture toughness of nuclear graphite NBG-18 using subsized specimens. *J Nucl Mater* 2011;412(3):315–20.
- [68] Burchell T, Erdman III D, Lowden RR, Hunter JA, Hannel CC, Campbell A. The Fracture Toughness of Nuclear Graphite Grades, Revision 1. Oak Ridge National Lab. (ORNL), Oak Ridge, TN (United States); 2022.